



**HAL**  
open science

# From real soils to 3D-printed soils : reproduction of complex pore network at the real size in a silty-loam soil

Nicola Dal Ferro, F Morari

## ► To cite this version:

Nicola Dal Ferro, F Morari. From real soils to 3D-printed soils : reproduction of complex pore network at the real size in a silty-loam soil. Soil Science Society of America, 2015. ird-01905147

**HAL Id: ird-01905147**

**<https://ird.hal.science/ird-01905147>**

Submitted on 25 Oct 2018

**HAL** is a multi-disciplinary open access archive for the deposit and dissemination of scientific research documents, whether they are published or not. The documents may come from teaching and research institutions in France or abroad, or from public or private research centers.

L'archive ouverte pluridisciplinaire **HAL**, est destinée au dépôt et à la diffusion de documents scientifiques de niveau recherche, publiés ou non, émanant des établissements d'enseignement et de recherche français ou étrangers, des laboratoires publics ou privés.



**From real soils to 3D-printed soils: reproduction of complex pore network at the real size in a silty-loam soil**

Journal:	<i>Soil Science Society of America Journal</i>
Manuscript ID:	S-2015-03-0097-OR.R2
Manuscript Type:	Papers on Original Research
Keywords:	X-ray computed microtomography , soil structure, 3D print, saturated hydraulic conductivity

SCHOLARONE™  
Manuscripts

View Only

1 **From real soils to 3D-printed soils: reproduction of complex pore network at the real size in a**  
2 **silty-loam soil**

3

4 N. Dal Ferro<sup>a</sup>, F. Morari<sup>a\*</sup>

5 *<sup>a</sup>Department of Agronomy, Food, Natural resources, Animals and Environment, Agripolis,*

6 *University of Padova, Viale Dell'Università 16, 35020 Legnaro (Padova), Italy*

7

8 **Abstract**

9 Pore complexity and micro-heterogeneity are pivotal in characterizing biogeochemical processes in  
10 soils. Recent advances in X-ray computed microtomography (microCT) allow the 3D soil  
11 morphology characterization of undisturbed samples, although its geometrical reproduction at very  
12 small spatial scales is still challenging. Here, by combining X-ray microCT with 3D multijet  
13 printing technology, we aimed to evaluate the reproducibility of 3D-printing soil structures at the  
14 original scale with a resolution of 80  $\mu\text{m}$  and compare the hydraulic properties of original soil  
15 samples with those obtained from the soil-like prototypes. Results showed that soil-like prototypes  
16 were similar to the original samples in terms of total porosity and pore shape. By contrast the pore  
17 connectivity was reduced by the incomplete wax removal from pore cavities after the 3D printing  
18 procedure. Encouraging results were also obtained in terms of hydraulic conductivity since  
19 measurements were successfully conducted on five out of six samples, showing positive correlation  
20 with experimental data. We are confident that future developments of 3D-printing technologies and  
21 of their combination with microCT will help to further the understanding of soil micro-  
22 heterogeneity and its effects on soil-water dynamics.

23

## 24 1. INTRODUCTION

25 The processes that form porous media lead to highly heterogeneous three-dimensional structures,  
26 forcing scientists to adopt models for reproducing the reality. This is the case for soil physics, which  
27 has its foundations laid on the capillary bundle model (Hunt et al., 2013). Water flow is still  
28 commonly conceptualized as a 2D bundle of cylindrical tubes passing through the soil only in the  
29 vertical direction, trivializing the natural complexity of a soil. As a result, derived models such as  
30 those of water conductivity (Burdine, 1953; Mualem, 1976) introduced empirical adjustments (e.g.  
31 a tortuosity factor) to compensate for fundamental errors in the conceptual model (Hunt et al.,  
32 2013). The simplification of reality in one-dimensional or two-dimensional models was supported  
33 by the inability to see and understand the 3D structure and its interactions with biota due to its  
34 opaque nature (Feeney et al., 2006). However, recent advanced technologies have provided a vast  
35 amount of data and their assimilation in more complex models that have partly superseded the use  
36 of reduction methods (Ahuja et al., 2006). The first steps for creating real-world situations in soil  
37 science used 3D random network models (e.g., Rajaram et al., 1997; Peat et al., 2000) that  
38 mimicked the soil complexity and dynamics in a three-dimensional space. In spite of their overall  
39 improvement in the understanding of matrix flow and transport of solutes, these models had two  
40 main limitations: a) computing limitations make some structural simplification unavoidable and b)  
41 the soil has such structural complexity that a reliable estimate of a representative elementary  
42 volume is difficult to quantify (Peat et al., 2000), as for most of the models. Lately, non-invasive  
43 imaging approaches have gained attention as they provide the opportunity to examine soil-water  
44 interactions from direct observations at the microscale. For example, the soil physical and chemical  
45 processes were replicated using high-tech materials with a refractive index similar to water,  
46 allowing the use of 3D optical microscopy in a transparent-reconstructed medium for the  
47 visualization of biophysical processes. Controlled experiments of how pore channels can influence

48 the biological and hydraulic dynamics can be realized, although the reconstructed medium is only  
49 partially reproducible because it is composed of single incoherent particles (Downie et al., 2012).

50 Impressive developments and insights into porous media research have also been provided by X-ray  
51 computed microtomography (microCT) that allows microscopic visualization of the spatial  
52 arrangement of complex structures (Cnudde and Boone, 2013). For the first time it became possible  
53 to investigate the interior of an object in a non-destructive way and to extract qualitative and  
54 quantitative information of multiphase porous materials (e.g., Tippkoetter et al., 2009; Mooney et  
55 al., 2012). In this context “digital rock physics”, i.e. the study of pore scale processes by the use of  
56 digital imaging and modelling, has expanded enormously the understanding of single and  
57 multiphase flow dynamics (Blunt et al., 2013).

58 Only recently 3D-printers have gained attention in the design of niche products, prototypes and one-  
59 time creations (e.g., Rangel et al., 2013), although the technology is 30-years old. This technology  
60 has been proposed in research as a tool to integrate virtual microCT information with real building  
61 models. In fact, the combination of such techniques make it possible to reconstruct complex  
62 microcosms with the heterogeneity discovered with microCT at a resolution of few micrometers,  
63 providing the opportunity to isolate the physical and chemical aspects that govern the  
64 biogeochemical and microbial processes in the soil (Otten et al., 2012; Ju et al., 2014; Bacher et al.,  
65 2015; Ringeisen et al., 2015). Nowadays, with 3D printing the diversified geometry encountered in  
66 a soil can be replicated at a resolution of tends of micrometers. Several materials can be used  
67 including plastics, resins, ceramics and metals.

68 Despite large uncertainties persisting about soil microscale heterogeneity and its effects on the  
69 macroscopic dynamics (Baveye et al., 2011), so far few have tried to combine high-resolution 3D  
70 imaging and printing technology to improve knowledge in soil science. In this study we combined  
71 3D printing technology with X-ray microCT in an attempt to reconstruct the 3D complexity of the

72 soil structure in a soil-derived model at the same spatial scale as the original one and test some  
73 hydraulic properties.

74

## 75 **2. MATERIAL AND METHODS**

### 76 *Experimental design and soil sampling*

77 The soil samples come from a long-term experiment established in 1962 at the experimental farm of  
78 the University of Padova (Italy). The soil (Table 1) is Fluvi-Calcaric Cambisol (CMcf), silty loam  
79 (FAO-UNESCO, 1990). This work considered soil samples from a long-term trial that compares  
80 two treatments: farmyard manure at  $60 \text{ t ha}^{-1} \text{ y}^{-1}$  (hereafter labelled “M”) and a no fertilization  
81 control (hereafter labelled “C”) on a continuous maize crop system. The same type of tillage has  
82 been used for both treatments, with autumn plowing and subsequent cultivations prior to sowing the  
83 main crop. The experimental layout is a randomized block with three replicates, on plots of  $7.8 \times 6$   
84 m. Further details on experimental design are extensively reported in the literature (e.g., Morari et  
85 al., 2006). A total of six undisturbed soil cores (5 cm diameter, 6 cm length) were collected in  
86 August 2010 (Fig. 1, step A), at the end of the maize season, from the topsoil (5 to 20 cm depth) in  
87 polymethylmethacrylate (PMMA) cylinders using a manual hydraulic core sampler (Eijkelkamp,  
88 The Netherlands). Cores were stored at  $5 \text{ }^\circ\text{C}$  until analysis.

89

### 90 *MicroCT soil scanning and image processing*

91 The pore structure of soil cores, labelled “M<sub>soil</sub>” and “C<sub>soil</sub>” for farmyard manure and no  
92 fertilization control, respectively (Fig. 1, step B) was sampled using X-ray computed  
93 microtomography (microCT). In order to allow the scanning of the whole soil core at a fine  
94 resolution, samples were analyzed at the “3S-R” facility in Grenoble (<http://www.3sr-grenoble.fr/>)

95 at a spatial resolution of 40  $\mu\text{m}$ . Setting parameters were 100 kV, 300  $\mu\text{A}$  and projections were  
96 collected during a 360° sample rotation at 0.3° angular incremental step. Each projection was the  
97 mean of 10 acquisitions and scan frequency was 7 images  $\text{s}^{-1}$ . Beam hardening artifacts were  
98 minimized during data acquisition using a 0.5 mm Al filter. In order to avoid pixel misclassification  
99 that might occur during projection measurements due to scattered radiation, nonlinearity of data  
100 acquisition systems, partial volume effects etc. (Hsieh, 2009), 2D projections were resized after  
101 acquisition using a mean filter by a two-pixel factor along the vertical and horizontal axis. As a  
102 result, the reconstructed images had a coarser resolution than that of acquisition (i.e. 80  $\mu\text{m}$ ).  
103 Resized projections were finally reconstructed using the dedicated software DigiCT 1.1 (Digisens,  
104 France) to obtain a stack of about 750 2D slices in 32-bit depth. 32-bit images were later converted  
105 into 8-bit depth.

106 The digital image processing and analysis of soil samples, conducted with the public domain image  
107 processing ImageJ (Vs. 1.45, National Institute of Health, <http://rsb.info.nih.gov/ij>), has already  
108 been reported in (Dal Ferro et al., 2013). Briefly, a cylindrical volume of interest with a diameter of  
109 600 pixels and composed of 600 slices (4.8 cm height  $\times$  4.8 cm diameter) was selected in order to  
110 exclude the PMMA sample holder. Slices were segmented using a global-threshold value based on  
111 the histogram greyscale that was determined by the maximum entropy threshold algorithm. The  
112 threshold value was selected where the inter-class entropy was maximized (Luo et al., 2010). 8-  
113 connectivity, a mathematical morphology closing operator (Serra, 1982), was applied to the binary  
114 images to fill misclassified pixels inside the pores as well as to maintain pore connections (Mooney  
115 et al., 2006). Successively, the one interconnected pore network (infinite cluster) that contained  
116 most of the porosity within each stack was extracted and analyzed with CTAn software v. 1.12.0.0  
117 (Bruker micro-CT, Kontich, Belgium) as this pore space was the only one to show continuity  
118 between the top and bottom of the soil cores. Although more connections between pores were likely  
119 present within the soil cores, microCT imaging provided only connections larger than the resolution

120 limits, restricting our analysis to the soil macroporosity. A description of the soil morphological  
121 parameters as a result of microCT scanning has already been reported in Dal Ferro et al. (2015)  
122 (Table 1).

123

#### 124 *3D mesh generation*

125 A surface mesh model for each sample (3 replicates  $\times$  2 treatments) was extracted from the one  
126 interconnected pore network that was identified from the microCT stacks using the free software  
127 InVesalius 3.0 (CTI, Campinas, São Paulo, Brazil) (Fig. 1, step G). The created model was then  
128 exported in the geometrical stereolithography file format encoded in Standard Tessellation  
129 Language (STL). The reconstructed STL model, composed of 10 to 30 million triangles depending  
130 on the complexity of the pore network, was visualized with the open-source software MeshLab  
131 v.1.3.2 (STI-CNR, Rome, Italy; <http://meshlab.sourceforge.net/>) in order to assess the continuity of  
132 pore connections along the vertical axis and successively simplified to a polygonal mesh that  
133 consisted of up to 10 million triangles. In order to compare the microCT imaging from the original  
134 samples with the 3D-printed prototypes from the STL model, one of the three replicate microCT  
135 stacks was selected for both “M” and “C”. Afterwards a volume of interest, corresponding to a  
136 cylinder of 300 pixels height  $\times$  300 pixels of diameter (Fig. 1, step C), was extracted by both  
137 samples (2.4 cm high  $\times$  2.4 cm diameter). InVesalius 3.0 was used to obtain a polygonal mesh  
138 model, from which a STL file was exported (Fig. 1, step D). MeshLab v.1.3.2 was used to simplify  
139 the polygonal mesh at two levels of detail, corresponding to 500 thousand (500k) and 10 million  
140 (10M) triangles respectively. Each model was 3D-printed twice (Fig. 1, step E), resulting in a total  
141 of eight models (2 soil samples  $\times$  2 generated meshes  $\times$  2 replicate printings). All the closed pores,  
142 i.e. the pores that had no connection to the space outside, were then digitally removed from the  
143 stacks since they cannot contribute to flow properties of the model.

144

145 *3D printing*

146 Lastly, 14 polygonal meshes (6 cylinders, 4.8 cm h × 4.8 cm diameter; 8 cylindrical subsamples, 2.4  
147 cm h × 2.4 cm diameter) were built with a commercial 3D printer. The printer (ProJet 3510 HD, 3D  
148 Systems, <http://www.3dsystems.com/>) was selected as it provided a fast prototype reconstruction  
149 with high resolution and available at a relatively low price (few hundred €). The 3D structure was  
150 printed with resin whose exact composition is proprietary but approximately contained an organic  
151 mixture of: ethoxylated bisphenol A diacrylate (15-35%), urethane acrylate oligomers (20-40 %),  
152 tripropyleneglycol diacrylate (1.5-3%) (Visijet Crystal, EX 200 Plastic material, Safety Data Sheet,  
153 [http://www.3dsystems.com](http://www.3dsystems.com/)). The 3D printer has a multijet printing technology, i.e. an inkjet  
154 printing process that deposits either photocurable plastic resin or casting wax materials layer by  
155 layer, with a spatial resolution of 29 μm and a declared accuracy of 25-50 μm, depending on  
156 building parameters and prototype size and geometry. The final result was a set of solid prototypes  
157 whose pores were filled with paraffin wax (the contact angle between water and wax, measured  
158 with a goniometer, was 120°), while the soil matrix was composed of the resin. The contact angle  
159 between the pure resin (cleaned of any wax) and the water, measured with a contact angle  
160 goniometer, was 69°.

161

162 *Wax removal procedure*

163 Wax removal is crucial in order to empty the pores and accurately replicate the complex geometry  
164 of the soil samples. Ultrasonication in oil at a temperature of 60 °C and 60 Hz for 24 h and oven  
165 drying at 60 °C until stabilized weight (*ca.* four days) were adopted as possible procedures to empty  
166 the pores. Alternative methods were considered: the use of xylene or vapor steam cleaning would  
167 have dissolved the wax, although it would have probably corrupted the solid pore surface, while  
168 alternative printing technologies without the use of wax as a physical support during 3d printing

169 were not feasible. As a result, we adopted a simple and relatively low-cost combination between 3D  
170 printing technology and cleaning procedure.

171

### 172 *3D prototypes scanning, image reconstruction and analysis*

173 The resulting prototypes from the sub-volume of the samples (i.e. “M<sub>small</sub>” and “C<sub>small</sub>” at a detail of  
174 500 thousand and 10 million triangles) were finally subjected to X-ray microCT scanning (Fig. 1,  
175 step F) in order to assess: a) the reproducibility and reliability of the 3D printing process; b) the  
176 smoothing effect of polygon reduction on the generated 3D structure; c) efficacy of the cleaning  
177 procedure to remove the wax from the pores. Prototypes were analyzed with a Skyscan 1172 X-ray  
178 microtomography (Bruker micro-CT, Kontich, Belgium) at the University of Padova since lower  
179 energy than those used for scanning the whole soil sample was required to penetrate the specimen.  
180 Setting parameters were 40 kV, 250  $\mu$ A and projections were collected during a 180° sample  
181 rotation at 0.25° angular incremental step. Each projection was the mean of eight acquisitions and  
182 scan frequency was 1.33 images s<sup>-1</sup>. Beam hardening artifacts were minimized during data  
183 acquisition using a 0.5 mm Al filter. The spatial resolution was 27  $\mu$ m. In order to avoid pixel  
184 misclassification that might occur during image acquisition (Hsieh, 2009), projections were resized  
185 after acquisition using a mean filter by a two-pixel factor along the vertical and horizontal axis. As a  
186 result, the reconstructed images had a final resolution twice that of acquisition (i.e. 54  $\mu$ m). Resized  
187 projections were reconstructed using the dedicated software NRecon v. 1.6.9.4 provided by Bruker  
188 micro-CT to obtain a stack of about 450 2D slices in 16-bit depth. 16-bit images were later  
189 converted into 8-bit depth.

190 Prototype matrix, wax and void phases were easily visualized and binarized with a single threshold  
191 level. 8-connectivity was applied to the binary images to fill misclassified pixels inside the pores as  
192 well as to maintain pore connections (Mooney et al., 2006). MicroCT porosity ( $\text{m}^3 \text{m}^{-3}$ ), pore size

193 distribution and open porosity (%), pore surface to volume ratio ( $\mu\text{m}^{-1}$ ), 3D fractal dimension and  
194 Euler number ( $\text{mm}^{-3}$ ) were estimated from each binarized stack using CTAn and compared with soil  
195 parameters obtained from the original sub-volume samples.

196

#### 197 *Hydraulic conductivity test on 3D-printed prototypes*

198 Saturated hydraulic conductivity ( $K_{s\text{-large}}$ ) measurements were conducted on the large prototypes  
199 (“M<sub>large</sub>” and “C<sub>large</sub>”, 4.8 cm high  $\times$  4.8 cm diameter) (Fig. 1, step H) by using a laboratory  
200 permeameter (Eijkelkamp, The Netherlands) that was adjusted to the size of the samples by using a  
201 gasket whose thickness created a seal at the interface between the prototype and the sample holder.  
202  $K_{s\text{-large}}$  was determined with both constant and variable head method, according to the hydraulic  
203 properties of the medium. As a rule of thumb,  $K_{s\text{-large}}$  values greater than  $5.8 \cdot 10^{-6} \text{ m s}^{-1}$  were easily  
204 determined by the constant head method, while the falling head method was conducted at smaller  
205  $K_{s\text{-large}}$  values. Before conducting the analysis and to ensure that water flowed only vertically from  
206 the top to the bottom of the prototypes, avoiding the loss of water from lateral pores, samples were  
207 firstly sealed with a plastic tape and successively coated with a layer of melted wax. As a result, it  
208 was ensured the complete sealing of the samples avoiding the lateral occlusion of interior pores.  
209 Successively samples were freely upward saturated at atmospheric pressure (water bath reached  $\frac{3}{4}$   
210 of sample height) using de-aerated water, then subjected to  $0.6 \cdot 10^{-5} \text{ Pa}$  to completely de-aerate them  
211 and saturated again as above.

212

#### 213 *Hydraulic conductivity test on original samples*

214 Saturated water conductivity on soil-like prototypes was compared with water flow calculated on  
215 the original soil samples and already proposed in (Dal Ferro et al., 2015). As a result, original  
216 samples were subjected to saturated water conductivity analyses ( $K_{s\text{-soil}}$ ,  $\text{m s}^{-1}$ ) using the constant

217 head or falling head method, depending on the soil properties and range of  $K_{s\text{-soil}}$  that can be  
218 measured (Reynolds et al., 2002). In addition, the microCT imaging dataset of the original samples  
219 (scanned at the “3S-R” facility in Grenoble) was used to calculate water conductivity on the one  
220 interconnected pore cluster ( $K_{\text{Morph}}$ ,  $\text{m s}^{-1}$ ) by using a morphologic approach as proposed by (Elliot  
221 et al., 2010). Briefly, the model consisted of combining three dimensional pore shape parameters  
222 with pore volume and using a modified Poiseuille equation as follows:

$$223 \quad Q = \frac{\pi R^4 \Delta P}{8 L_c \nu}, \quad [1]$$

224 where  $R$  is pore radius,  $\nu$  is the viscosity of water at room temperature,  $\Delta P$  is the change in  
225 hydrostatic pressure and  $L_c$  is the pore length, depending on pore shape characteristics.

226 Lastly, rearrangement of Darcy’s law allowed the  $K_{\text{Morph}}$  estimation for the extracted pore network:

$$227 \quad K = \frac{QL}{A\Delta P}, \quad [2]$$

228 where  $A$  is the cross-sectional area of the sample and  $L$  is the sample length. A detailed description  
229 of the methods and results for the soils proposed here can be found in Dal Ferro et al. (2015).

230

### 231 **3. RESULTS**

#### 232 *Soil volume and prototype measurements*

233 Ultrasonication in oil was only partially able to remove the wax from pores, while the subsequent  
234 oven drying at 60 °C was able to remove most of it (Fig. 2). A further increase in temperature was  
235 not possible because, according to the manufacturer, it would have weakened the resin structure or  
236 melted part of it. As a result, the combination of both techniques was used as the best procedure  
237 currently available to successfully empty the open pores as well as maintain the solid structure.

238 However, the continuing advances in 3D-printing technology and the use of heat-resistant materials  
239 will allow the full removal of the support material (e.g. by evaporation).

240 Soil porosity of sub-volumes scanned with microCT (“M<sub>soil</sub>” and “C<sub>soil</sub>” 2.4 cm high × 2.4 cm  
241 diameter) was entirely connected to the space outside the soil matrix (open pores/total porosity =  
242 100%), but highly different between “M<sub>soil</sub>” (0.114) and “C<sub>soil</sub>” (0.036) (Table 2). The open pores of  
243 “M<sub>small</sub>” prototypes were slightly lower than porosity detected by microCT, with negligible changes  
244 between 500 thousand (500k) and 10 million (10M) triangle meshes. Indeed, only 2.4% of microCT  
245 porosity (0.109 and 0.110 in 500k and 10M, respectively) was confined within the solid phase  
246 (Table 2). By contrast, the “C<sub>small</sub>” prototypes showed a consistent increase of confined pores with  
247 respect to the total ones, ranging from 15.1% in the 500k to 18.4% in the 10M meshes, on average.  
248 As a result, the “C<sub>soil</sub>” porosity (0.036) was slightly greater than “C<sub>small</sub>” built both from 500  
249 thousand (0.024) and 10 million (0.027) triangle meshes respectively.

250 Pore size distribution (PSD) curves (Fig. 4), measured on microCT images in volumetric terms  
251 according to the medial-axes determination and sphere-fitting measurement (Remy and Thiel,  
252 2002), were distributed differently between “M” and “C”. In “M” the most frequent pore classes  
253 were distributed between 240 μm and 560 μm diameter, while they were shifted towards smaller  
254 pores in “C”, ranging between 160 μm and 440 μm. Comparable data were found between PSD  
255 prototype classes, in both “M” and “C”, with negligible variations between replicates and meshes.  
256 By contrast, a sharp increase of the small pores was observed in the original samples with respect to  
257 the prototypes: this was particularly clear for pore classes smaller than 800 μm and 490 μm in  
258 “M<sub>soil</sub>” and “C<sub>soil</sub>”, where the integral of the PSD differences was around 30% and 10% of microCT  
259 porosity, respectively. Finally, it was noticed that some pores were still filled with wax despite its  
260 melting and removal with ultrasonication and oven drying (Fig. 3). In particular, wax most resided  
261 in thin throats (< 200 μm, on average) between largest cavities, leading to their disconnection and  
262 thus increasing both the average size of empty pores and the number of isolated ones.

263 Pore morphological features (Table 2), estimated by means of pore surface/volume ratio ( $\mu\text{m}^{-1}$ ),  
264 Euler number (i.e. an indicator of pore connectivity, where the greater is the value, the lower is the  
265 pore connectivity;  $\text{mm}^{-3}$ ) (Vogel et al., 2010) and 3D fractal dimension (box-counting method)  
266 (Perret et al., 2003), emphasized the self-similarity between the prototypes that were generated by  
267 the same original sub-volume. For instance, the pore surface/volume ratio was  $0.007 \mu\text{m}^{-1}$  in  
268 “M<sub>small</sub>” prototypes as characterized by different meshes (500k and 10M triangles), while the fractal  
269 dimension (2.42 and 2.25 in the original “M<sub>soil</sub>” and “C<sub>soil</sub>”, respectively) ranged in “M<sub>small</sub>”  
270 between 2.10 (500k triangles) and 2.62 (10M triangles) and in “C<sub>small</sub>” between 2.38 (500k  
271 triangles) and 2.55 (10M triangles). Only the Euler number parameter, particularly in “M<sub>small</sub>” and  
272 “C<sub>small</sub>” built from 500k triangle meshes, showed high variability between the prototypes (Table 2).

273

#### 274 *Experimental saturated hydraulic conductivity measurements on large prototypes*

275 Experimental saturated hydraulic conductivity ( $K_{s\text{-large}}$ ) data were obtained on five of the six  
276 reconstructed large prototypes (“M<sub>large</sub>” and “C<sub>large</sub>” 4.8 cm high  $\times$  4.8 cm diameter, an example is  
277 reported in Fig. 5) since water did not flow through one of the “C<sub>large</sub>” samples (Table 3).  $K_{s\text{-large}}$   
278 was generally higher in “M” ( $18.5 \text{ m s}^{-1}$ , on average) than “C” ( $0.035 \text{ m s}^{-1}$ , on average), ranging  
279 between a minimum of  $0.023 \text{ m s}^{-1}$  observed in “C” and a maximum of  $13.5 \text{ m s}^{-1}$  in “M. The water  
280 flow measurements on the prototypes were generally greater ( $7.65 \cdot 10^{-5} \text{ m s}^{-1}$ , on average) than those  
281 measured ( $K_{s\text{-soil}} = 3.59 \cdot 10^{-6}$ , on average) and modelled ( $K_{\text{Morph}} = 1.91 \cdot 10^{-6} \text{ m s}^{-1}$ ) on the original soil  
282 samples (Table 3) (Dal Ferro et al., 2015). Finally, positive correlations were observed between  
283 soil-like  $K_{s\text{-large}}$  values and both  $K_{s\text{-soil}}$  ( $R^2 = 0.69$ ) and  $K_{\text{Morph}}$  ( $R^2 = 0.93$ , Fig. 6).

284

## 285 **4. DISCUSSION**

286 The comparison between morphological characteristics of replicated small prototypes (“M<sub>small</sub>” and  
287 “C<sub>small</sub>”) showed that 3D printing technology was able to retain the basic features of the macropore  
288 network. More specifically, the pore size and shape characteristics of the largest pores was easily  
289 visualized on the microCT imaging (Fig. 3), highlighting the similarity between reconstructed  
290 models. Moreover, introducing some smoothing of the surface walls by the simplification of the  
291 mesh (500 thousand vs. 10 million triangles) did not show significant changes between macropore  
292 characteristics. In particular, the “M” microCT porosity and pore surface/volume ratio had a  
293 coefficient of variation of 3.6% and 4.8%, respectively. These results were supported by others:  
294 Otten et al. (2012) reported a very high reproducibility of twelve prototypes since the measured  
295 porosity (0.66) was characterized by a very low coefficient of variation (3.36%), although their soil-  
296 like prototypes were scaled up three times with respect to the original size of the soil samples. By  
297 contrast, our prototypes were reconstructed at the real size, although the soil microscale  
298 heterogeneity that was provided by the fine silt and clay particles could not be faithfully reproduced  
299 due to the microCT soil scanning (40  $\mu\text{m}$ ) and 3D printing resolution limits (29  $\mu\text{m}$ ).

300 The successful reproduction of generated “M<sub>small</sub>” prototypes (Fig. 1, step E) was partly reappraised  
301 by evaluating the pore morphological characteristics in detail (Table 2). In fact, the pore structure  
302 parameters varied between the reconstructed models, especially in the “C<sub>small</sub>” prototypes. For  
303 instance, the coefficient of variation of total porosity was 11.5% in the “C<sub>small</sub>” prototypes,  
304 increasing to 63% in the Euler number. Nevertheless, it is worth noticing that the microCT scanning  
305 of small prototypes (Fig. 1, step F) was performed at a resolution (27  $\mu\text{m}$ ) that was finer than that  
306 used during the 3D-printing (29  $\mu\text{m}$ ,  $\pm$  50  $\mu\text{m}$ ), emphasizing the systematic errors during the model  
307 building process. As a result, the mismatch observed between soil samples (“M<sub>soil</sub>” and “C<sub>soil</sub>”) and  
308 prototypes (“M<sub>small</sub>” and “C<sub>small</sub>”) structures were the result of the combined effect between: a) soil  
309 digital imaging due to microCT scanning; b) inaccuracy during the 3D printing process; c)  
310 prototype digital imaging due to microCT scanning. Furthermore, the 3D mesh generation created

311 distorted elements from the voxel-based microCT volumes, although the negligible variations  
312 between small prototypes as printed from 500 thousand and 10 million triangles suggested their  
313 minor role during the prototypes production. Moreover, the partial effectiveness of wax removal  
314 from the macropores (Fig. 3), quantified at around 2.4% (“ $M_{small}$ ”) and 16.7% (“ $C_{small}$ ”) of microCT  
315 porosity, increased the uncertainty on the pore quantity and morphology. Finally, the biggest  
316 differences were observed in terms of Euler number, showing its ability to identify slight structure  
317 changes between replicated prototypes. The wax entrapped in the voids created a discontinuity  
318 between adjacent pores by modifying the degree of connection of the macropore network and partly  
319 isolating them from the space outside the solid matrix. As a result, the soil volumes (“ $M_{soil}$ ” and  
320 “ $C_{soil}$ ”) generally had both a higher microCT total porosity and a lower Euler number (i.e. more  
321 connections) than the reconstructed prototypes (Table 2). As suggested by the pore size distribution  
322 analysis, the wax was easily removed from the largest pores, while it consistently remained in the  
323 smallest ones (Fig. 4). Finally, a mismatch between soil and soil-like porosity was probably  
324 introduced during microCT soil analysis and the following mesh generation. Indeed microCT  
325 imaging was composed of cubic voxels while polygonal mesh comprised a surface triangulation,  
326 avoiding their full overlap.

327 In spite of the difficulty in totally cleaning the wax from the macropores, measurements of saturated  
328 hydraulic conductivity were successfully conducted on five of the six large prototypes. Only the  
329 saturated conductivity measurement on one “ $C_{large}$ ” prototype failed. Since one of the “ $C_{large}$ ” soil-  
330 derived model was characterized by the lowest total porosity (0.015), most likely the entrapped wax  
331 occluded the scarce conductive pores within the whole prototype and prevented flow. Water flow  
332 measurements, calculated through the one interconnected macropore network that spanned the  
333 sample, were highly correlated with properties calculated on the original samples ( $K_{s-soil}$ ) and  
334 particularly with those modelled ( $K_{Morph}$ ) on the same pore network (Fig. 6) (Dal Ferro et al., 2015).  
335 Nevertheless,  $K_{s-large}$  had higher values than  $K_{s-soil}$  and  $K_{Morph}$  by at least one order of magnitude in

336 the “M” treatment (Table 3), although the total porosity had been reduced with respect to the soil  
337 sample ones in two ways: a) the prototypes were reconstructed on the basis of digital imaging from  
338 microCT scanning that performed at a resolution that excluded all the small connections between  
339 the largest pores and decreased the adsorption along the macropore walls; b) part of microCT  
340 porosity was probably still filled with wax during  $K_{s-large}$  measurements, reducing the water flow  
341 capacity of the porous medium. These results suggested the major role of conducting macropores on  
342 water flow dynamics (Jarvis, 2007), although the undetected and unprinted micropores  $< 80 \mu\text{m}$   
343 might have partially increased  $K_{s-large}$  to approach the experimental  $K_{s-soil}$  (Elliot et al., 2010),  
344 particularly when the soil structure was largely composed of thin pores and microcracks are often  
345 insufficiently imaged with microCT and thus underrepresented (i.e. in the control samples),  
346 especially in the vicinity of grain contacts (Andrä et al., 2013). Some smoothing of the pore  
347 surfaces, introduced during the prototype generation, decreased the friction factor between the  
348 liquid and solid phases with respect to the original samples, as was shown by the results of pore  
349 surface/volume ratio (Table 2). This would have reduced the pressure drop (Kumar et al., 2011) at  
350 high  $K_{s-large}$  values, obeying the dynamics on the viscous forces as described in the Stokes  
351 equations, while with low water velocity the difference between  $K_{s-large}$  and  $K_{s-soil}$  and  $K_{Morph}$  was  
352 strongly reduced. By contrast, the contact angle between the water and the solid walls ( $69^\circ$ ) was  
353 only a minor factor for influencing the water movement, although it is reasonable that, despite the  
354 emptying procedure, the pores were still coated with wax that would have induced fluid slip for  
355 water flowing over a hydrophobic surface (Tretheway and Meinhart, 2002).

356

## 357 5. CONCLUSIONS

358 Integrating X-ray microtomography and 3D printing technology is feasible in soil science at the  
359 microscale and provides great opportunities to better understand the role of micro-heterogeneity in  
360 the soil-water dynamics. In particular, soil-like prototypes were built with relatively large

361 replicability and similarity to the original ones at the actual size, with a resolution of 80  $\mu\text{m}$ .  
362 Moreover, the mesh simplification (from 100 million to 500 thousand triangles) did not reveal  
363 significant differences between prototypes. By contrast, the full wax removal from the pores was  
364 not completely solved as it limited the pore connectivity and increased the surface smoothing.  
365 Nevertheless, water conductivity was successfully performed on five of the six large prototypes,  
366 showing a strong correlation with experimental and modelled data from the original soil samples.  
367 The comparison between  $K_{s\text{-large}}$  (i.e. on prototypes) and  $K_{\text{Morph}}$  (morphologic model) data,  
368 performed on the same porous systems, highlighted the major role of the macropore surface  
369 smoothing and the hydrophobic nature of wax. In particular, an increase of fluid slip and  
370 consequently of water velocity at laminar flow was observed for  $K_{s\text{-large}} \geq 10^{-5} \text{ m s}^{-1}$ , while it was  
371 consistently reduced at lower values. By contrast, the detection of micropores  $< 80 \mu\text{m}$  would have  
372 approached the  $K_{s\text{-large}}$  values to reach the experimental ones ( $K_{s\text{-soil}}$ ), especially at low water  
373 velocities. In order to promote a broad application of 3D prototypes in the hydrological research,  
374 future application of 3D printing technology should address many technological challenges. In fact  
375 a higher microCT scanning and 3D-printed resolution will favor the representation of the soil pore  
376 system at the nanoscale and its heterogeneity. Moreover the use of soil-like materials will be able to  
377 model the physical-chemical interaction between water and the pore surface. Nevertheless, even at  
378 this stage, our work suggests as 3D printing technology can represent a breakthrough technology for  
379 the study of soil structure and its interaction with biogeochemical processes.

380

381

## 382 REFERENCES

383 Ahuja, L.R., L. Ma, and D.J. Timlin. 2006. Trans-disciplinary soil physics research critical to  
384 synthesis and modeling of agricultural systems. *Soil Sci. Soc. Am. J.* 70:311-326.  
385 doi:10.2136/sssaj2005.0207

- 386 Andrä, H., N. Combaret, J. Dvorkin, E. Glatt, J. Han, M. Kabel, Y. Keehm, F. Krzikalla, M. Lee,  
387 and C. Madonna. 2013. Digital rock physics benchmarks-part II: Computing effective properties.  
388 *Comput. Geosci.* 50:33-43. doi:10.1016/j.cageo.2012.09.008
- 389 Baveye, P.C., D. Rangel, A.R. Jacobson, M. Laba, C. Darnault, W. Otten, R. Radulovich, and  
390 F.A.O. Camargo. 2011. From dust bowl to dust bowl: soils are still very much a frontier of science.  
391 *Soil Sci. Soc. Am. J.* 75:2037-2048. doi:10.2136/sssaj2011.0145
- 392 Bacher, M., Schwen, A., and Koestel, J. 2015. Three-dimensional printing of macropore networks  
393 of an undisturbed soil sample. *Vadose Zone J.* 14:1-10. doi:10.2136/vzj2014.08.0111
- 394 Blunt, M.J., B. Bijeljic, H. Dong, O. Gharbi, S. Iglauer, P. Mostaghimi, A. Paluszny, and C.  
395 Pentland. 2013. Pore-scale imaging and modelling. *Adv. Water Resour.* 51:197-216. doi:  
396 10.1016/j.advwatres.2012.03.003
- 397 Burdine, N.T. 1953. Relative permeability calculations from pore size distribution data. *J. Pet.*  
398 *Technol.* 5:71-78. doi:http://dx.doi.org/10.2118/225-G
- 399 Cnudde, V., and M.N. Boone. 2013. High-resolution X-ray computed tomography in geosciences:  
400 A review of the current technology and applications. *Earth-Sci. Rev.* 123:1-17.  
401 doi:10.1016/j.earscirev.2013.04.003
- 402 Dal Ferro, N., P. Charrier, and F. Morari. 2013. Dual-scale micro-CT assessment of soil structure in  
403 a long-term fertilization experiment. *Geoderma* 204:84-93. doi:10.1016/j.geoderma.2013.04.012
- 404 Dal Ferro, N., A.G. Strozzi, C. Duwig, P. Delmas, P. Charrier, and F. Morari. 2015. Application of  
405 smoothed particle hydrodynamics (SPH) and pore morphologic model to predict saturated water  
406 conductivity from X-ray CT. *Geoderma* 255:27-34. doi:10.1016/j.geoderma.2015.04.019
- 407 Downie, H., N. Holden, W. Otten, A.J. Spiers, T.A. Valentine, and L.X. Dupuy. 2012. Transparent  
408 soil for imaging the rhizosphere. *PloS ONE.* 7:e44276. doi:10.1371/journal.pone.0044276
- 409 Elliot, T.R., W.D. Reynolds, and R.J. Heck. 2010. Use of existing pore models and X-ray computed  
410 tomography to predict saturated soil hydraulic conductivity. *Geoderma* 156:133-142.  
411 doi:10.1016/j.geoderma.2010.02.010
- 412 FAO-UNESCO. 1990. Soil map of the world. Revised Legend. FAO, Rome.

- 413 Feeney, D.S., J.W. Crawford, T. Daniell, P.D. Hallett, N. Nunan, K. Ritz, M. Rivers, and I.M.  
414 Young. 2006. Three-dimensional microorganization of the soil–root–microbe system. *Microb. Ecol.*  
415 52:151-158. doi:10.1007/s00248-006-9062-8
- 416 Hsieh, J. 2009. *Computed tomography: Principles, design, artifacts, and recent advances*. Second  
417 ed. SPIE Bellingham, Washington, USA.
- 418 Hunt, A.G., R.P. Ewing, and R. Horton. 2013. What's wrong with soil physics? *Soil Sci. Soc. Am.*  
419 J. 77:1877-1887. doi:10.2136/sssaj2013.01.0020
- 420 Jarvis, N.J. 2007. A review of non-equilibrium water flow and solute transport in soil macropores:  
421 principles, controlling factors and consequences for water quality. *Eur. J. Soil Sci.* 58:523-546.  
422 doi:10.1111/j.1365-2389.2007.00915.x
- 423 Ju, Y., H. Xie, Z. Zheng, J. Lu, L. Mao, F. Gao, and R. Peng. 2014. Visualization of the complex  
424 structure and stress field inside rock by means of 3D printing technology. *Chin. Sci. Bull.* 59:5354-  
425 5365. doi:10.1007/s11434-014-0579-9
- 426 Kumar, V., M. Paraschivoiu, and K.D.P. Nigam. 2011. Single-phase fluid flow and mixing in  
427 microchannels. *Chem. Eng. Sci.* 66, 1329-1373. doi:10.1016/j.ces.2010.08.016
- 428 Luo, L., H. Lin, S. Li. 2010. Quantification of 3-D soil macropore networks in different soil types  
429 and land uses using computed tomography. *J. Hydrol.* 393:53-64.  
430 doi:10.1016/j.jhydrol.2010.03.031
- 431 Mooney, S.J., C. Morris, and P.M. Berry. 2006. Visualization and quantification of the effects of  
432 cereal root lodging on three-dimensional soil macrostructure using X-ray computed tomography.  
433 *Soil Sci.* 171:706-718. doi:10.1097/01.ss.0000228041.03142.d3
- 434 Mooney, S.J., T.P. Pridmore, J. Helliwell, and M.J. Bennett. 2012. Developing X-ray Computed  
435 Tomography to non-invasively image 3-D root systems architecture in soil. *Plant Soil.* 352:1-22.  
436 doi:10.1007/s11104-011-1039-9
- 437 Morari, F., E. Lugato, A. Berti, and L. Giardini. 2006. Long-term effects of recommended  
438 management practices on soil carbon changes and sequestration in north-eastern Italy. *Soil Use*  
439 *Manage.* 22:71-81. doi:10.1111/j.1475-2743.2005.00006.x
- 440 Mualem, Y. 1976. A new model for predicting the hydraulic conductivity of unsaturated porous  
441 media. *Water Resour. Res.* 12:513-522. doi:10.1029/WR012i003p00513

- 442 Otten, W., R. Pajor, S. Schmidt, P.C. Baveye, R. Hague, and R.E Falconer. 2012. Combining X-ray  
443 CT and 3D printing technology to produce microcosms with replicable, complex pore geometries.  
444 *Soil Biol. Biochem.* 51:53-55. doi:10.1016/j.soilbio.2012.04.008
- 445 Peat, D.M.W., G.P. Matthews, P.J. Worsfold, and P.J., and S.C Jarvis. 2000. Simulation of water  
446 retention and hydraulic conductivity in soil using a three-dimensional network. *Eur. J. Soil Sci.*  
447 51:65-79. doi:10.1046/j.1365-2389.2000.00294.x
- 448 Perret, J.S., S.O. Prasher, and A.R. Kacimov. 2003. Mass fractal dimension of soil macropores  
449 using computed tomography: from the box-counting to the cube-counting algorithm. *Eur. J. Soil*  
450 *Sci.* 54:569-579. doi:10.1046/j.1365-2389.2003.00546.x
- 451 Rajaram, H., L.A. Ferrand, and M.A. Celia. 1997. Prediction of relative permeabilities for  
452 unconsolidated soils using pore-scale network models. *Water Resour. Res.* 33:43-52.  
453 doi:10.1029/96WR02841
- 454 Rangel, D.P., C. Superak, M. Bielschowsky, K. Farris, R.E. Falconer, and P.C. Baveye. 2013.  
455 Rapid prototyping and 3-D printing of experimental equipment in soil science research. *Soil Sci.*  
456 *Soc. Am. J.* 77:54-59. doi:10.2136/sssaj2012.0196n
- 457 Remy, E., Thiel, E., 2002. Medial axis for chamfer distances: computing look-up tables and  
458 neighbourhoods in 2D or 3D. *Pattern Recogn. Lett.* 23:649-661. doi:10.1016/S0167-  
459 8655(01)00141-6
- 460 Reynolds, W.D., D.E. Elrick, E.G. Youngs, A. Amoozegar, H.W.G. Booltink, and J. Bouma. 2002.  
461 3.4 Saturated and field-saturated water flow parameters. p. 797-801. In J.H. Dane and G.C. Topp  
462 (ed.) *Methods of Soil Analysis Part 4 - Physical Methods*. SSSA Madison, WI
- 463 Ringeisen, B.R., K. Rincon, L.A. Fitzgerald, P.A. Fulmer, and P.K. Wu. 2015. Printing soil: a  
464 single-step, high-throughput method to isolate micro-organisms and near-neighbour microbial  
465 consortia from a complex environmental sample. *Methods Ecol. Evol.* 6:209-217.  
466 doi:10.1111/2041-210X.12303
- 467 Serra, J. 1992. *Image analysis and mathematical morphology*. Academic Press, London, UK.
- 468 Tippkoetter, R., T. Eickhorst, H. Taubner, B. Gredner, and G. Rademaker. 2009. Detection of soil  
469 water in macropores of undisturbed soil using microfocus X-ray tube computerized tomography  
470 ( $\mu$ CT). *Soil Till. Res.* 105:12-20. doi:10.1016/j.still.2009.05.001

471 Tretheway, D.C., and C.D. Meinhart. 2002. Apparent fluid slip at hydrophobic microchannel walls.  
472 Phys. Fluids. 14:L9-L12. doi:0.1063/1.1432696

473 Vogel, H.J., U. Weller, and S. Schlüter. 2010. Quantification of soil structure based on Minkowski  
474 functions. Comput. Geosci. 36:1236-1245. doi:10.1016/j.cageo.2010.03.007

475

For Review Only

476 **Captions of figures**

477 **Figure 1** Outline of steps used to obtain soil-like prototypes and sample measurements.

478 **Figure 2** 2D slices from microCT imaging (M = farmyard manure; C = control) of original soil  
479 samples (A1, B1) and soil-like prototypes after the wax removal procedure with ultrasonication  
480 (A2, A3, B2, B3) and oven drying (A4, B4).

481 **Figure 3** 2D slices from microCT imaging of original soil samples (A1, B1) and soil-like  
482 prototypes (M = farmyard manure; C = control). Prototypes were obtained in duplicate from a  
483 polygonal mesh composed of both 500 thousand (500k; A2, A5, B2, B5) and 10 million (10M; A3,  
484 A6, B3, B6) triangles. Grayscale images are composed of empty pores (black objects) and solid  
485 material (gray objects). Binary images are composed of empty pores (white) and solid material  
486 (black).

487 **Figure 4** Pore size distribution estimated by means of X-ray microCT on original soil samples  
488 (“M<sub>soil</sub>” and “C<sub>soil</sub>”) and on soil-like prototypes (“M<sub>small</sub>” and “C<sub>small</sub>”) from 3D printing at different  
489 mesh accuracy (500k = 500 thousand triangles; 10M = ten million triangles).

490 **Figure 5** 3D representations of a large soil sample (farmyard manure treatment) as a result of X-ray  
491 microCT analysis (A, C; spatial resolution of 40 μm) and pictures of its 3D-printed copy (B, D;  
492 spatial resolution of 29 μm).

493 **Figure 6** Relationship between saturated water conductivities estimated on soil-like prototypes ( $K_{s-}$   
494  $_{large}$ , m s<sup>-1</sup>) and on the original soil samples by means of (A) experimental ( $K_{s-soil}$ , m s<sup>-1</sup>) and (B)  
495 modelling ( $K_{Morph}$ , m s<sup>-1</sup>) approach.

496 **Table 1** Texture and microCT pore morphological parameters of original soil cores (4.8 cm high × 4.8 cm diameter). Standard error values are  
 497 reported in brackets.

ID	Replicate	Soil physical properties				MicroCT parameters			
		Sand (%)	Silt (%)	Clay (%)	Total porosity <sup>a</sup> (m <sup>3</sup> m <sup>-3</sup> )	MicroCT porosity (m <sup>3</sup> m <sup>-3</sup> )	Mean pore diameter <sup>b</sup> (μm)	Pore surface/volume (μm <sup>-1</sup> )	Euler number (mm <sup>-3</sup> )
M	1	32.1	63.3	4.7	0.490	0.086	783.74	0.008	0.31
M	2	32.0	63.3	4.7	0.461	0.102	530.24	0.011	1.09
M	3	30.0	65.0	5.0	0.476	0.045	883.97	0.009	0.16
Average		31.4(0.7)	63.9(0.6)	4.8(0.1)	0.476(0.008)	0.078(0.017)	732.65(105.26)	0.009(0.001)	0.52(0.29)
C	1	27.5	65.7	6.7	0.459	0.015	386.96	0.011	0.16
C	2	37.8	57.2	5.0	0.432	0.020	338.58	0.014	0.6
C	3	32.6	62.0	5.4	0.439	0.033	374.06	0.013	3.13
Average		32.6(3.0)	61.6(2.5)	5.7(0.5)	0.443(0.008)	0.023(0.005)	366.53(14.46)	0.013(0.001)	1.65(1.21)

498 <sup>a</sup>Gravimetric method with water saturation.

499 <sup>b</sup>Weighted mean of soil pore size distribution.

500

501 **Table 2** 3D parameters from microCT scanning of original soil volumes (“M<sub>soil</sub>” and “C<sub>soil</sub>”) and soil-like prototypes (“M<sub>small</sub>” and “C<sub>small</sub>”). Soil  
 502 and soil-like volumes were 2.4 cm high × 2.4 cm diameter. Standard error values are reported in brackets.

503

ID	Sample scanned	Mesh <sup>a</sup>	MicroCT porosity (m <sup>3</sup> m <sup>-3</sup> )	Open pores/total porosity (%)	Mean pore diameter <sup>b</sup> (μm)	Pore surface/volume (μm <sup>-1</sup> )	Euler number (mm <sup>-3</sup> )	3D fractal dimension
M <sub>soil</sub>	Soil	-	0.114	100.00	858.60	0.007	0.42	2.41
M <sub>small</sub>	Prototype	500k	0.113	98.97	925.60	0.007	3.54	2.61
M <sub>small</sub>	Prototype	500k	0.106	96.36	943.26	0.007	0.82	2.10
M <sub>small</sub>	Prototype	10M	0.113	98.71	940.04	0.007	1.70	2.62
M <sub>small</sub>	Prototype	10M	0.107	96.32	953.31	0.007	0.97	2.17
Average	Prototype	-	0.110 (0.002)	97.591(0.84)	940.55(6.62)	0.007(0.000)	1.758(0.72)	2.38(0.16)
C <sub>soil</sub>	Soil	-	0.036	100.00	319.02	0.014	0.33	2.25
C <sub>small</sub>	Prototype	500k	0.027	90.30	397.66	0.013	0.981	2.40
C <sub>small</sub>	Prototype	500k	0.022	79.59	393.33	0.013	0.171	2.55
C <sub>small</sub>	Prototype	10M	0.028	86.35	380.00	0.013	0.795	2.38
C <sub>small</sub>	Prototype	10M	0.025	76.90	246.21	0.026	1.509	2.46
Average	Prototype	-	0.026(0.002)	83.28(3.54)	354.30(41.83)	0.016(0.004)	0.864(0.319)	2.45(0.04)

504 <sup>a</sup>500k = 500 thousand triangle mesh; 10M = 10 million triangle mesh.

505 <sup>b</sup>Weighted mean of soil-like prototypes pore size distribution.

506

507

508 **Table 3** Experimental saturated conductivity values ( $K_{s\text{-large}}$ ,  $\text{m s}^{-1}$ ) estimated on soil-like prototypes (“ $M_{\text{large}}$ ” and “ $C_{\text{large}}$ ”, 4.8 cm high  $\times$  4.8 cm  
 509 diameter) and compared with experimental ( $K_{s\text{-soil}}$ ) and modelled ( $K_{\text{Morph}}$ ) ones on the original soil samples. Standard error values are reported in  
 510 brackets.

511

ID	Replicate	$K_{s\text{-large}}$ ( $10^{-6} \text{ m s}^{-1}$ )	$K_{s\text{-soil}}^{\text{a}}$ ( $10^{-6} \text{ m s}^{-1}$ )	$K_{\text{Morph}}^{\text{a}}$ ( $10^{-6} \text{ m s}^{-1}$ )
M	1	134.94	6.31	5.17
M	2	19.46	2.41	4.13
M	3	30.50	3.41	1.74
Average		61.63 (36.79)	4.04 (1.17)	3.68 (1.02)
C	1	N/A	5.27	0.04
C	2	0.23	2.22	0.16
C	3	0.47	1.90	0.24
Average		0.35(0.12)	3.13(1.07)	0.15(0.06)

512 <sup>a</sup>data from Dal Ferro et al. (2015).

513

514

515

516

517

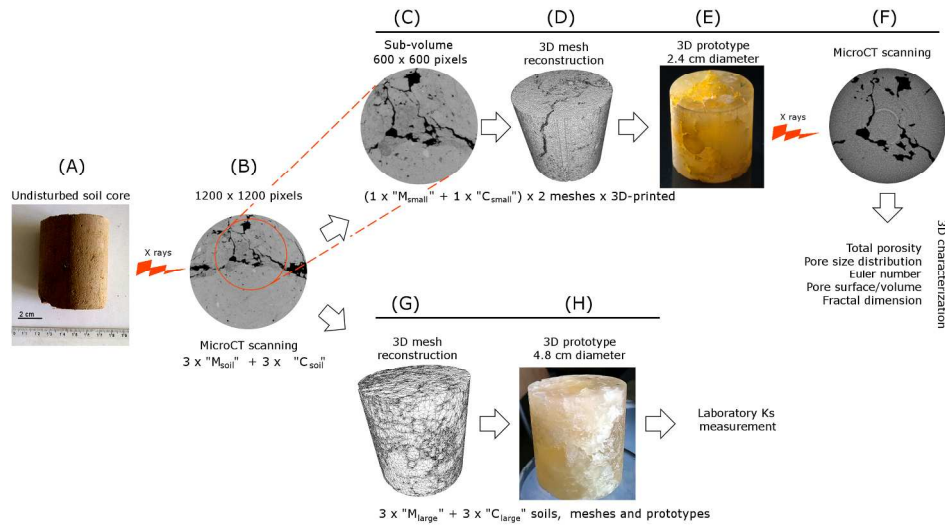


Figure 1 Outline of steps used to obtain soil-like prototypes and sample measurements. 216x127mm (300 x 300 DPI)

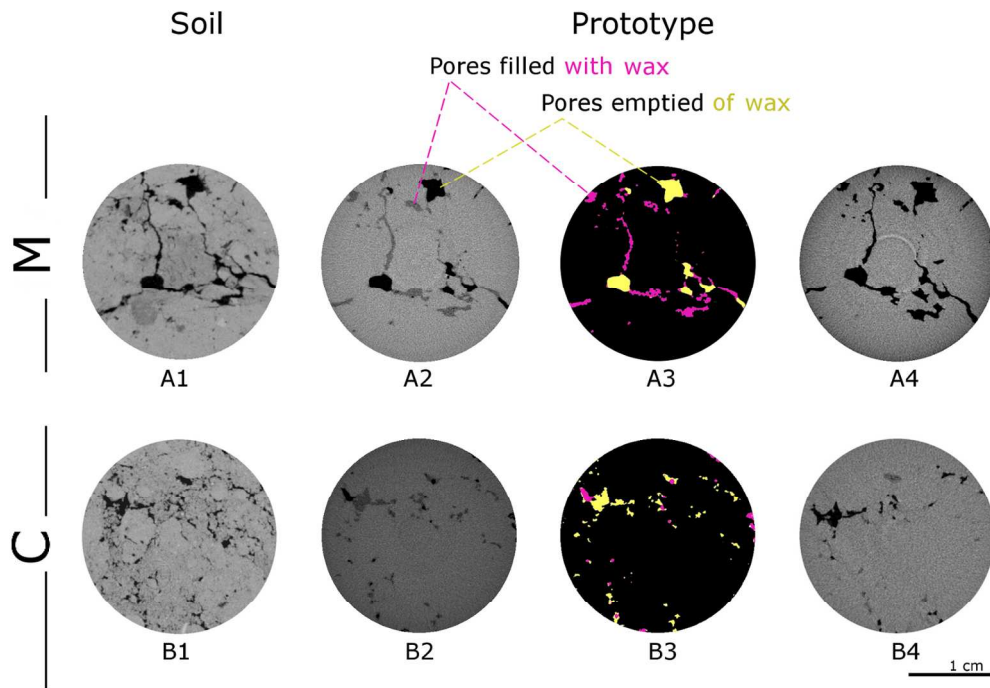


Figure 2: 2D slices from microCT imaging (M = farmyard manure; C = control) of original soil samples (A1, B1) and soil-like prototypes after the wax removal procedure with ultrasonication (A2, A3, B2, B3) and oven drying (A4, B4).  
152x111mm (300 x 300 DPI)

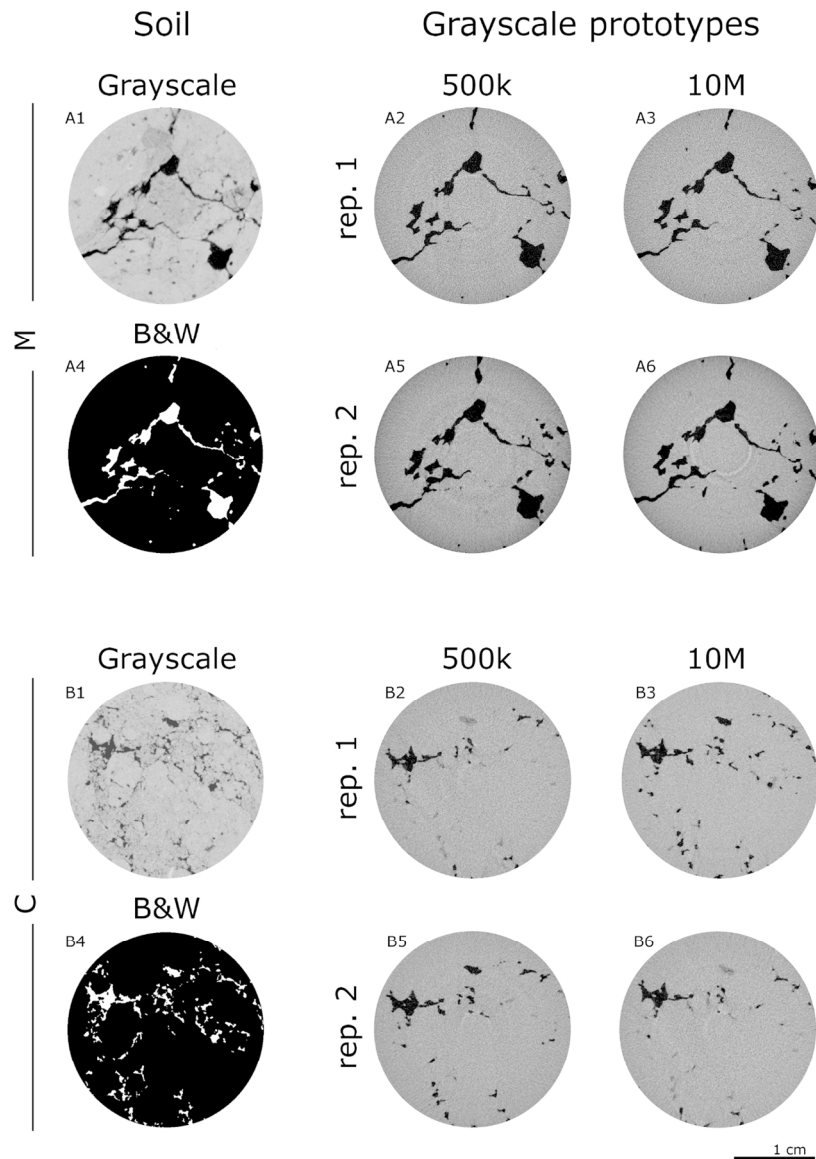


Figure 3 2D slices from microCT imaging of original soil samples (A1, B1) and soil-like prototypes (M = farmyard manure; C = control). Prototypes were obtained in duplicate from a polygonal mesh composed of both 500 thousand (500k; A2, A5, B2, B5) and 10 million (10M; A3, A6, B3, B6) triangles. Grayscale images are composed of empty pores (black objects) and solid material (gray objects). Binary images are composed of empty pores (white) and solid material (black).  
119x160mm (300 x 300 DPI)

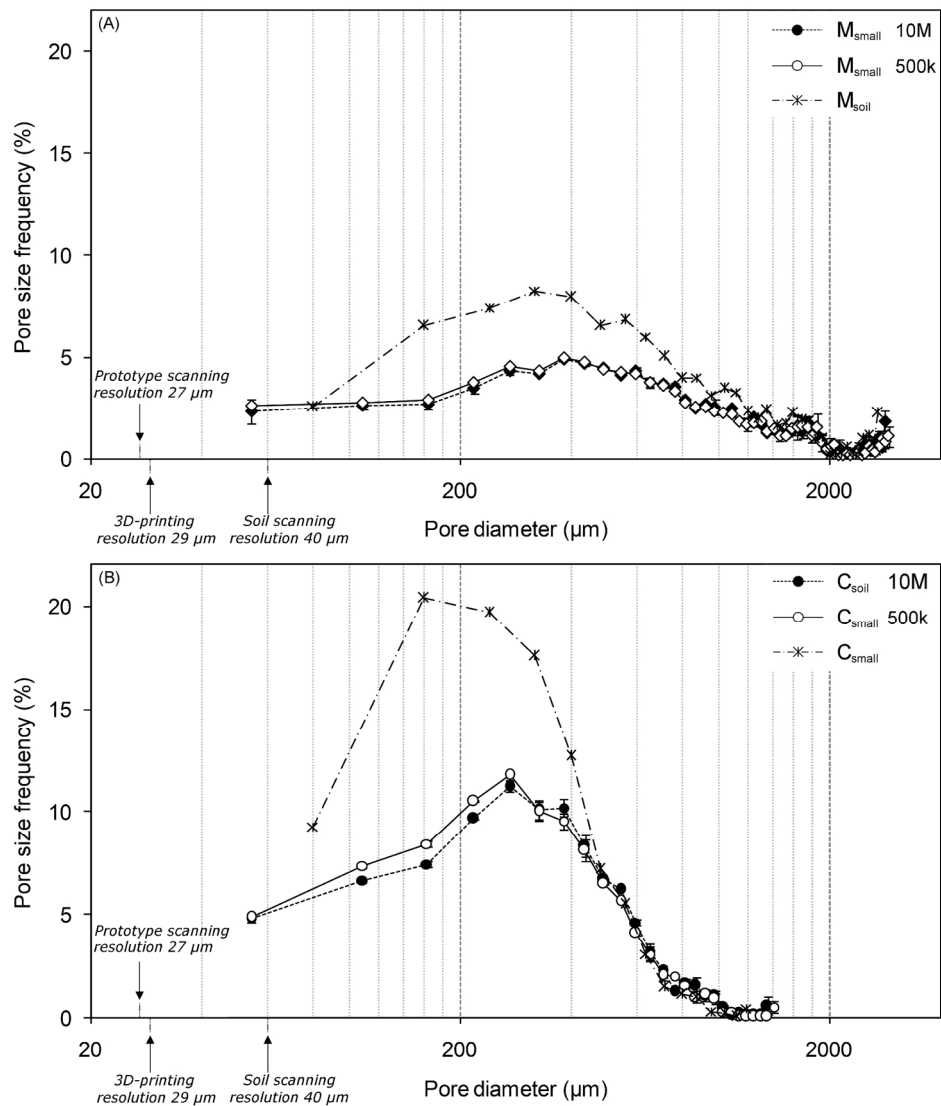


Figure 4: Pore size distribution estimated by means of X-ray microCT on original soil samples ("Msoil" and "Csoil") and on soil-like prototypes ("Msmall" and "Csmall") from 3D printing at different mesh accuracy (500k = 500 thousand triangles; 10M = ten million triangles).  
169x197mm (300 x 300 DPI)

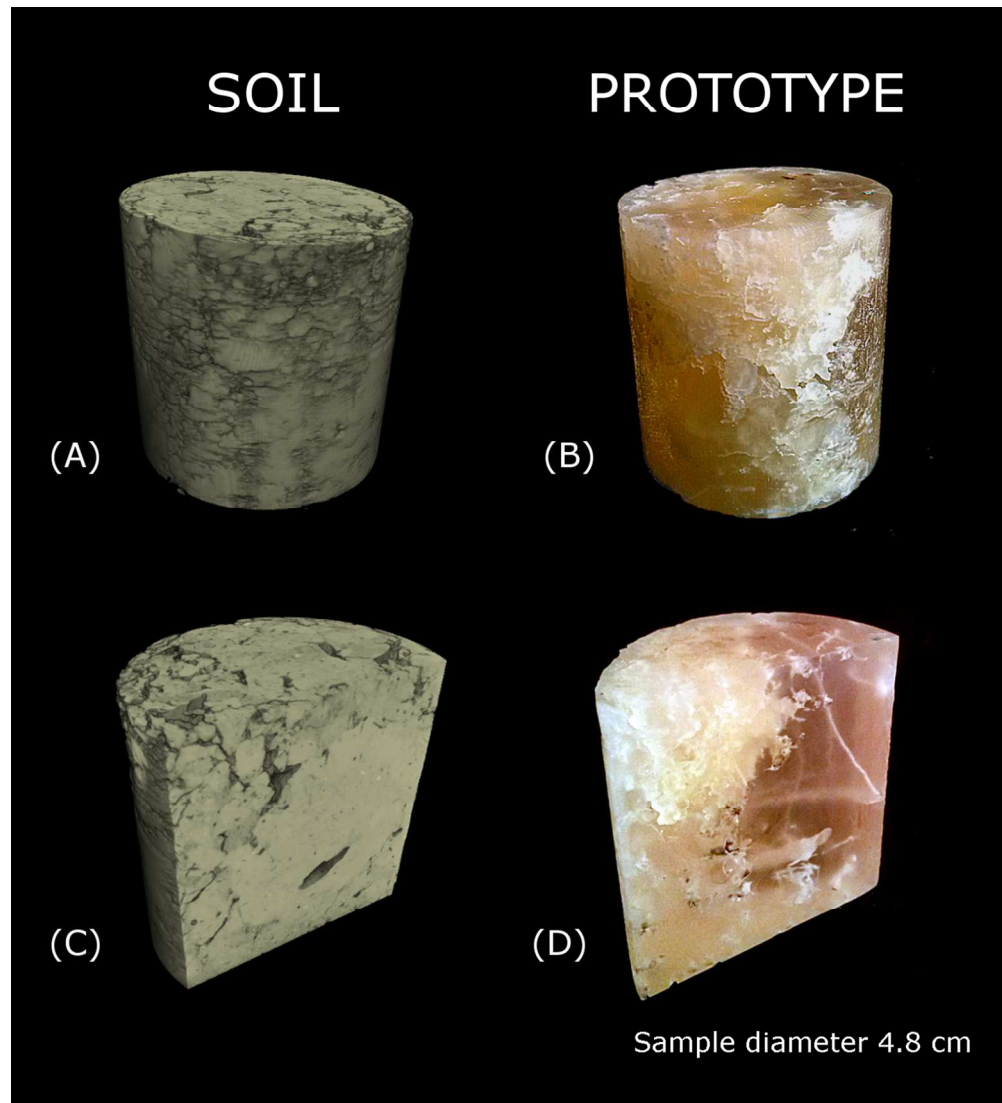


Figure 5: 3D representations of a large soil sample (farmyard manure treatment) as a result of X-ray microCT analysis (A, C; spatial resolution of 40  $\mu\text{m}$ ) and pictures of its 3D-printed copy (B, D; spatial resolution of 29  $\mu\text{m}$ ).  
118x130mm (300 x 300 DPI)

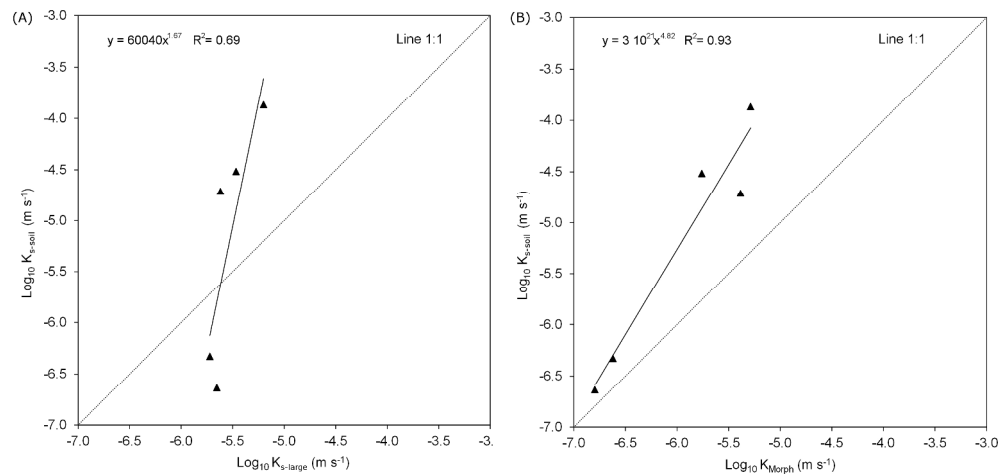


Figure 6 Relationship between saturated water conductivities estimated on soil-like prototypes ( $K_{s\text{-large}}$ ,  $\text{m s}^{-1}$ ) and on the original soil samples by means of (A) experimental ( $K_{s\text{-soil}}$ ,  $\text{m s}^{-1}$ ) and (B) modelling ( $K_{\text{Morph}}$ ,  $\text{m s}^{-1}$ ) approach.  
317x152mm (300 x 300 DPI)